Title	Dielectric charge control in electrostatic MEMS positioners / varactors
Authors(s)	Blokhina, Elena, Lopez, David, Gorreta, Sergi, Molinero, David, Feely, Orla, Pons Nin, Joan, Dominguez, Manuel
Publication date	2012-02-06
Publication information	Blokhina, Elena, David Lopez, Sergi Gorreta, David Molinero, Orla Feely, Joan Pons Nin, and Manuel Dominguez. "Dielectric Charge Control in Electrostatic MEMS Positioners / Varactors." IEEE, February 6, 2012. https://doi.org/10.1109/JMEMS.2011.2182500.
Publisher	IEEE
Item record/more information	http://hdl.handle.net/10197/3615
Publisher's statement	Personal use of this material is permitted. Permission from IEEE must be obtained for all other uses, in any current or future media, including reprinting/republishing this material for advertising or promotional purposes, creating new collective works, for resale or redistribution to servers or lists, or reuse of any copyrighted component of this work in other works.
Publisher's version (DOI)	10.1109/JMEMS.2011.2182500

Dielectric Charge Control in Electrostatic MEMS Positioners / Varactors

Elena Blokhina[1], David Lopez[2], Sergi Gorreta[2], David Molinero[2], Orla Feely[1], Joan Pons-Nin[2], Manuel Dominguez-Pumar[2*]

[1] School of Electrical, Electronic and Mechanical Engineering, University College Dublin, Ireland
[2] Micro and Nano Technologies Group, Universitat Politécnica de Catalunya, Spain

[*] corresponding author email: manuel.dominguez@upc.edu

***Abstract*—A new dynamical closed-loop method is proposed to control dielectric charging in capacitive MEMS positioners/varactors for enhanced reliability and robustness. Instead of adjusting the magnitude of the control voltage to compensate the drift caused by the dielectric charge, the method uses a feedback loop to maintain it at a desired level: the device capacitance is periodically sampled and bipolar pulses of constant magnitude are applied. Specific models describing the dynamics of charge and a control map are introduced. Validation of the proposed method is accomplished both through discrete-time simulations and with experiments using MEMS devices that suffer from dielectric charging.**

***Index Terms*—MEMS control, dielectric charging control, MEMS reliability**

I. Introduction

In recent years, the use of electrostatic MEMS devices has been extended to a wide set of applications, including RF components, resonators, micromirrors, capacitive sensors, etc. However the commercial use of these devices is hindered by reliability problems limiting their lifetime [1]. Typical structures of capacitive MEMS devices include silicon oxide and nitride as the most common dielectric materials (see the recent review [2] and references cited there). For those capacitive MEMS, the charge accumulated in dielectric layers has a significant impact on the behaviour of such devices by altering the electric field distribution in the gap and causing offset shifts in the capacitance-voltage (C–V) characteristic, as is shown, for instance, in [3]–[6]. Thus, detection and control of dielectric charge are of capital importance due to their strong influence on device performance and reliability.

It is well known that many insulating layers demonstrate carrier conduction when the electric field or temperature is sufficiently high. Types of conduction mechanisms depend fundamentally on the specific materials and on the strength of the applied electric field [7], [8]. The problem of dielectric charging has been actively studied over recent decades, and certain progress has been achieved (see, for instance, [1] and literature cited there). The charging dynamics strongly depends on the dielectric type, the applied voltage and the architecture of the system. It involves many physical mechanisms, not all of which are fully understood, but it is commonly accepted that charge is injected from one of the electrodes and trapped within the dielectric [9], [10]. Dielectric charging can be found in RF MEMS as well as in other types of micro devices where dielectric materials contacting with metals are a part of their topologies [11]–[13].

With the accumulation of experimental data, theoretical and modelling results, several methods that allow the prevention or elimination of the dielectric charge have begun to appear in the literature. Refs. [14]–[16] develop and validate through experimental fitting a phenomenological model for dielectric charging and discharging under either positive or negative applied voltages in RF MEMS switches. According to this, waveform signal changes [17] and periodic switching of voltage polarity [14]–[16] have been proposed and demonstrated as promising ways to reduce the effects of dielectric charging. Indeed, since the electrostatic force is attractive, MEMS devices can be actuated by either positive or negative voltages. In this approach, the dielectric charge may be ”compensated” since bipolar voltages cause opposite effects in dielectric: charge injection and extraction.

However, open-loop methods still exhibit long term reliability problems. For instance, since the charging behaviours under the different polarities are not symmetrical, a small amount of net charge still accumulates under equal positive and negative duty cycles (i.e. see [18]). In this situation a closed-loop dynamical control can be more effective and robust.

An example of a method employing closed-loop elements of control and bipolar voltages for the specific case of MEMS switches working at given ON/OFF regimes (beyond and before pull-in) can be found in [18], [19]. This method monitors the pull-out voltage shift of the device in order to decide the sign of the voltage to be applied the next time it is pulled down. This means that the time intervals between application of voltages may vary as a function of how the device is scheduled to be working in the down or up positions. Unless some time restrictions apply to the distribution and duration of the periods in the down and up positions, it may not be possible to guarantee a stable value of charge during the whole time the device is operated. For example, all the time the device is constantly being used in the down (or up) position no control is applied to the charge. Large variations of charge may be expected if this time is long compared with the time constants involved in the charging process.

In this paper we propose a new control scheme to fix the dielectric charge to a desired level for MEMS devices working in the OFF state, such as varactors or electrostatic positioners. The method senses in real time the capacitance drift of the

MEMS due to dielectric charging and it dynamically adjusts the ratio of positive and negative voltage duty cycles in order to fix the amount of charge. This control scheme is inspired by sigma-delta modulation: the position (i.e. the input capacitance) of the device is periodically sampled and, after each sampling time, a positive or a negative bias voltage is applied, depending on whether the position is above or below a reference value.

In fact, the proposed method can be seen as a control of the position of the electrostatic MEMS that indirectly provides a control of the dielectric charge. The time constants involved in the process are very different. Changes in the position of the MEMS can be achieved in microseconds, whereas the dielectric charging time constants can be quite large in comparison. In this way, the control of the position of the device is loose (the device will be moving while changing the applied voltages), but the charge is kept almost constant, once stable regimes are achieved. Typical of a feedback control, this scheme has the additional benefit of guarding against drift due to other effects such as mechanical fatigue and temperature change, thereby making the MEMS device not only more reliable, but also more robust.

The paper is organized as follows. Section II of this paper introduces the set of ordinary differential equations used to describe the dynamics of MEMS devices similar to those used in our experiments. It includes three different ”phenomenological” models, commonly used in the literature, for describing the dynamics of the charge trapped in the dielectric layer under positive and negative voltages. Since the control method proposed works in discrete time, in section III we introduce and validate discrete-time equations (maps) as a more efficient analysis tool than differential equations. The effectiveness of the control method in limiting the amount of trapped charge is first validated through discrete-time simulations in section IV. Here we show that for all charging and discharging models considered in this work, the algorithm is capable of fixing the charge in the dielectric. Experimental validation of the control method is presented in section V.

II. Statement of the Problem

In this section, we introduce the electromechanical model used to describe our MEMS devices. We point out that we do not consider an equivalent circuit model for the MEMS. Instead, we describe the movable part by a mechanical equation where the dielectric charge affects electrostatic force. Next, models for dielectric charge dynamics are added to make the system of equations self-consistent. Finally, we introduce the charge control algorithm and validate the charge models through comparison with experimental data.

A. Electromechanical Model

A schematic view of an voltage driven MEMS with a movable top electrode is shown in Fig. 1. Using a typical mass-spring-damper ordinary differential equation (ODE), the dynamics of the deflection of the upper electrode $x(t)$ can be described as follows:

$$m\ddot{x}(t) + b\dot{x}(t) + kx(t) = F_{el}(x, t) \tag{1}$$

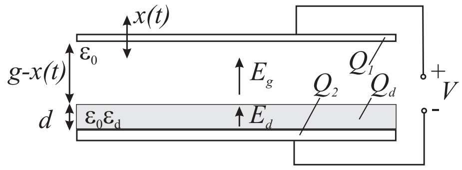

Fig. 1. Schematic view of an electrostatic MEMS with a movable top electrode and a dielectric layer on the fixed bottom electrode.

where F_{el} is the electrostatic force applied to the movable electrode, m its mass, b the damping factor and k the effective spring constant.

In order to obtain a simple model of the electrostatic force F_{el} for devices with homogeneous distribution of charge of one sign, let us assign the instantaneous charges $Q_1(t)$, $Q_2(t)$ and $Q_d(t)$ to the top and bottom electrodes and to the top of the dielectric layer respectively. This approach follows [3], but here we assume that charges are functions of time. Anyway, after the first introduction of time-dependent variables, we will drop the notation $f(t)$, still assuming that these variables depend on time.

For an electrically neutral system, one can write that

$$Q_1 + Q_2 + Q_d = 0 \tag{2}$$

Applying Gauss' Law, the electric fields in the air gap and in the dielectric (see Fig. 1) are found to be

$$E_g(t) = -\frac{Q_1}{A\varepsilon_0}\,, \quad E_d(t) = \frac{Q_2}{A\varepsilon_0\varepsilon_d} = -\frac{Q_1 + Q_d}{A\varepsilon_0\varepsilon_d} \tag{3}$$

where ε_0 is the air permittivity, ε_d is the relative permittivity of the dielectric, A is the area of the upper electrode, g is the equilibrium gap and d is the thickness of the dielectric layer.

The voltage drop $V(t)$ can be calculated by integrating the electric field across the device, from the bottom electrode (at $z = 0$) to the top (at $z = d + g - x$)

$$\begin{aligned} V(t) &= -\int_0^d E_d\,dz - \int_d^{d+g-x} E_g\,dz = \\ &= -E_d d - E_g(g - x) = \frac{Q_1 + Q_d}{C_d} + \frac{Q_1}{C_g(t)} \end{aligned} \tag{4}$$

Here the capacitance of the gap is $C_g(t) = A\varepsilon_0/(g-x)$, the constant capacitance of the dielectric layer is $C_d = A\varepsilon_0\varepsilon_d/d$. Thus, with $C_{g,0} = \varepsilon_0 A/g$, the total MEMS capacitance is

$$C(t) = C_g||C_d = \frac{A\varepsilon_0\varepsilon_d}{d + \varepsilon_d(g - x)} = \frac{C_{g,0}}{1 - \frac{x}{g} + \frac{C_{g,0}}{C_d}} \tag{5}$$

Now one can obtain the charge at the top electrode Q_1 as a function of the parasitic charge Q_d as

$$Q_1 = \left(V - \frac{Q_d}{C_d}\right)C \tag{6}$$

and, finally, express the electrostatic force applied to the top electrode as

$$F_{el} = -\frac{Q_1 E_g}{2} = \frac{Q_1^2}{2A\varepsilon_0} = \frac{C^2}{2A\varepsilon_0}(V - \frac{Q_d}{C_d})^2 \tag{7}$$

Here we draw attention to the sign of the parasitic charge. The electrostatic force for a given voltage V increases and, consequently, the pull-in voltage decreases when some amount of negative charge $Q_d < 0$ is stored in the dielectric. This agrees with results from the literature [6], [20], [21].

Expression (7) is a particular case of the most general one obtained in [22], where non-planar electrodes and non-homogeneous distributions of charges in the dielectric are considered. The term in brackets of (7) is often referred to as the voltage shift due to the parasitic charge

$$V_{shift} = \frac{Q_d}{C_d} \tag{8}$$

making $V - V_{shift}$ the effective voltage applied to the electrode. Measuring V_{shift} is one of the most common techniques carried out in experiments, since this simple relation allows one to determine the dielectric charge.

B. Dielectric Charge Model

In order to make the model self-consistent, equations describing the evolution of the dielectric charge Q_d must be provided together with (1) and (7). Since charge build-up is a very complex process that may involve many mechanisms, we aim at a "phenomenological" model that describes qualitatively the dynamics of the charge. Then, this section introduces and briefly reviews the most common charging and discharging laws found in the literature.

While constructing the models, we will keep in mind two things. Firstly, the dielectric can accumulate charges of both polarities, positive and negative, depending on the applied voltage. Secondly, it has been found in [20] that for specific devices used in our experiments the source of charge is the bottom electrode when high electric fields are applied, and that the trapped charge is negative for $V > 0$. We will formulate the model and the control method considering charge of both signs, but we will mostly focus on the case of negative charge while presenting the results. Therefore, to formulate the model we will use two sets of expressions: charging with negative Q_d^n and discharging of the positive Q_d^p charge at $V > 0$, and, vice versa, discharging of the negative and charging with the positive charge at $V < 0$. Thus, the total accumulated charge is a *superposition* of such charges

$$Q_d(t) = Q_d^n(t) + Q_d^p(t) \tag{9}$$

Below, we describe the three models of the dielectric charge dynamics that we incorporate into the mechanical equation.

1) Model A — Exponential Dynamics: The dynamics of the charge of one sign resembles an exponential, $Q(t) = A_0 + A_1 \exp(-t/\tau)$, where the constants A_0 and A_1 are found from experimental data fitting and time constant τ represents the characteristic time scale of the process.

Since we require the charge dynamics at both polarities of the voltage, we will redefine A_0 and A_1. We introduce the saturation levels Q_{max}^n and Q_{max}^p eventually reached by negative and positive charges. For simplicity, we use here the initial conditions such that the charging processes start from zero $Q^{n,p}(0) = 0$ and the discharging processes start from the maximum value $Q^{n,p}(0) = Q_{max}^{n,p}$ Therefore, we obtain the equations

$$Q_d^n = \begin{cases} Q_{max}^n(1 - e^{-t/\tau_C^n}) & V > 0 \\ Q_{max}^n e^{-t/\tau_D^n} & V < 0 \end{cases} \tag{10}$$

$$Q_d^p = \begin{cases} Q_{max}^p e^{-t/\tau_D^p} & V > 0 \\ Q_{max}^p(1 - e^{-t/\tau_C^p}) & V < 0 \end{cases} \tag{11}$$

where $\tau_C^{n,p}$ and $\tau_D^{n,p}$ are the charging and discharging constants for negative and positive charges.

In the most general case, there may be any arbitrary negative and positive charges accumulated in the dielectric by the time $t_0 : Q_0 = Q^n(t_0) + Q^p(t_0),\ t_0 > 0$. The form involving Q_0 and t_0 is very convenient for constructing iterative (discrete-time) equations and we discuss it in detail in the next section. We describe eqs. (10)-(11) as *Model A*.

In [23], dielectric charging is described by the exponential law and obtained using a simple electronic circuit. Works [14], [16], [24], [25] use this law, among others, to fit experimental data. However, all papers admit that this model captures basic features, such as saturation of the charge and the characteristic time for charging, but displays discrepancies from realistic charging curves at short time scales when the charging process has just started.

2) Model B — Multi-exponential Dynamics: The extension of Model A is a superposition of exponentials with different time constants τ_i: $Q = A_0 + A_1 e^{-t/\tau_1} + A_2 e^{-t/\tau_2} + ...$ In our case, we will take the form of the model from [14], with maximum levels $Q_{max,i}^{n,p}$ for each ith component of negative and positive charges, such that the total maximum is $Q_{max}^{n,p} = \sum_i Q_{max,i}^{n,p}$. We also introduce the coefficients $\zeta_i^{n,p} = Q_{max,i}^{n,p} / Q_{max}^{n,p}$ and present the charging and discharging dynamics as

$$Q_d^n = \begin{cases} Q_{max}^n - \sum_i \zeta_i^n Q_{max}^n e^{-t/\tau_{Ci}^n} & V > 0 \\ \sum_i \zeta_i^n Q_{max}^n e^{-t/\tau_{Di}^n} & V < 0 \end{cases} \tag{12}$$

$$Q_d^p = \begin{cases} \sum_i \zeta_i^p Q_{max}^p e^{-t/\tau_{Di}^p} & V > 0 \\ Q_{max}^p - \sum_i \zeta_i^p Q_{max}^p e^{-t/\tau_{Ci}^p} & V < 0 \end{cases} \tag{13}$$

which we denote as *Model B*. Note that, according to the definition, $\sum_i \zeta_i^{n,p} = 1$.

The superposition model is extensively developed in [14], [21], [26]. It is based on measurements of the transient charging and discharging currents of MEMS switches in the ON state, when they resemble Metal-Insulator-Metal (MIM) capacitors. In these works, the superposition model with only two time constants τ_1 and τ_2 shows a good agreement with experiments and it is used later to develop bipolar actuation waveforms [15], [16]. Model B with two time constants was also obtained from accurate fitting of experimental data in [11] for a single crystal silicon resonator. Moreover, superposition models with two time constants are successfully employed to fit experimental results in other recent papers [25], [27].

3) Model C — Stretched Exponential Dynamics: The charge dynamics is described as: $Q(t) = A_0 + A_1 e^{-(t/\tau)^\beta}$, where $0 < \beta < 1$. In contrast with Models A and B, this law involves 'non-linear' time t^β. Let us take the conventional form often found in literature as *Model C*

$$Q_d^n = \begin{cases} Q_{max}^n \left(1 - e^{-(t/\tau_C^n)^{\beta_C^n}}\right) & V > 0 \\ Q_{max}^n e^{-(t/\tau_D^n)^{\beta_D^n}} & V < 0 \end{cases} \tag{14}$$

$$Q_d^p = \begin{cases} Q_{max}^p \left(1 - e^{-(t/\tau_C^p)^{\beta_C^p}}\right) & V > 0 \\ Q_{max}^p e^{-(t/\tau_D^p)^{\beta_D^p}} & V < 0 \end{cases} \tag{15}$$

In [28], the stretched exponential law appears from the assumption that traps in a dielectric layer have a continuous distribution in the time scale $\int_0^\infty \rho(\tau)\exp(-t/\tau)d\tau$.

The transient capacitance in the ON and OFF states of a MEMS device was well fitted by the stretched exponential law in [29]–[31], where authors point out that the study of polarization effects may be very important for certain devices. In these works, the capacitance is related to the dielectric charge through a simple expression, and both are described as stretched exponential functions of time. In [30], the appearance of the stretched exponential is related to the Williams-Watts-Kohlrausch relaxation law in amorphous dielectric materials.

We note that non-saturation models are suggested in the literature. For example, in [32] the voltage drift as a function of time does not saturate. In addition, Herfst et al [24], [33], while applying the exponential, stretch exponential and square root models to fit experimental data, note that $\sqrt{t}$ accurately describes the voltage shift versus time. The square root itself is a non-saturation function, however, these works note that it might appear as a Taylor expansion of the stretched exponential with $\beta \approx 0.5$.

Since we assume that the dielectric cannot accumulate an infinite amount of charge, we will consider Models A, B and C given by (10)-(11), (12)-(13) and (14)-(15) respectively as the models of the charge dynamics. They all display saturation for each sign of charge, given by $Q_{max}^{n,p}$. The dynamics of the square root from [24] can be simulated by Model C with an appropriate time constant and a very large saturation level.

C. Dielectric Charge Control for Capacitive MEMS

Due to the fact that the dynamics of the trapped charge strongly depend on the sign of the applied voltage, it has been demonstrated in [14], [16] that the parasitic charge effects can be mitigated by using bipolar voltage waveforms. The problem is that these are open loop control methods, i.e. no sensing is performed in order to decide which voltage should be applied. Moreover, since dielectric layers exhibit radically different charge time constants, depending on the materials and the fabrication processes, open loop methods do not perform "perfect" charge compensations, and thus the devices still exhibit drift effects after a certain number of actuation cycles.

To address this problem, we propose a method to dynamically control the amount of parasitic charge stored in the dielectric. It measures the device capacitance at each sampling time and compares it with a given threshold value C_{th}. If the measured capacitance remains below the threshold, it applies a positive or 'charge' voltage V_{ch}, thus injecting charge into the dielectric layer. Otherwise, if the measured capacitance is above the threshold value, it applies a negative or 'discharge' voltage V_{disch}, thus removing charge from the dielectric.

Then, defining V_n as the voltage applied after the sampling time nT_s, one can write

$$V_n = \begin{cases} V_{ch} & \text{if} \quad C_n < C_{th} \\ V_{dis} & \text{if} \quad C_n > C_{th} \end{cases} \tag{16}$$

where $C_n = C(nT_s)$ is the total MEMS capacitance (5) measured and x_n is the position of the device at the n^{th} sampling time

$$C_n = \frac{C_{g,0}}{1 - \frac{x_n}{g} + \frac{C_{g,0}}{C_d}} \tag{17}$$

Though we develop our theory, simulate and demonstrate the control method for a device with an open gap in the regime of a varying capacitance, we see that the method can be eventually extended to devices operating in switching mode. For example, for devices that are prone to strong charging or that discharge slowly, the method can be applied in OFF, to reduce the charge introduced during a previous ON state to a minimal level faster than by simply applying a zero voltage.

D. Validation of Charging and Discharging Dynamics

Three different models describing charge dynamics have been considered and discussed in this section. On the other hand, the charge control method, based on the complementary effects of bipolar voltages, has been also introduced. In order to ensure the applicability of the models under bipolar voltage actuation schemes, several fittings with experimental data have been performed. Three devices with silicon nitride as dielectric layer, but made with two different technologies, PolyMUMPS and a specific process from our clean room, are considered here.

It is also important to note that Models A, B and C appear as models of the dielectric charge dynamics for switches forming MIM capacitors [16], [24], [25]. Since we develop our theory with the open gap, it is a strong motivation for us to validate these models for our devices.

In the experiments, the MEMS capacitance as a function of time, $C(t)$, was monitored. The voltage sequence applied is as follows: 1) zero voltage 2) positive voltage V_{ch} and 3) negative voltage V_{dis}. Since our devices accumulate negative charge, the capacitance grows while V_{ch} is being applied and it eventually tends to the corresponding saturation level. When V_{dis} is applied, the capacitance displays a sharp jump and starts growing again, tending to its level as if $Q_d = 0$. An example of this behaviour is shown in fig. 2, where the thick gray line is the capacitance transient measured and the dashed gray line is the capacitance level for $V_{ch} = |V_{dis}| = 6\,V$ and $Q_d = 0$. Let us note that from this level $C(t)$ starts growing at charging and to this level it returns after discharging.

Fig. 2 clearly shows that the dielectric layer accumulates only negative charge. Indeed, if there was positive charge, application of a negative voltage would cause its build-up in the

TABLE I
FITTING PARAMETERS FOR MODEL B

Device 1 (fig. 2)			
τ_{C1}	110 s	τ_{C2}	15 s
τ_{D1}	70 s	τ_{D2}	20 s
ζ_1	0.2	ζ_2	0.8

Device 2			
τ_{C1}	4600 s	τ_{C2}	200 s
τ_{D1}	4600 s	τ_{D2}	200 s
ζ_1	0.2	ζ_2	0.8

Device 3 (fig. 4)			
τ_C	12000 s	β_C	0.25

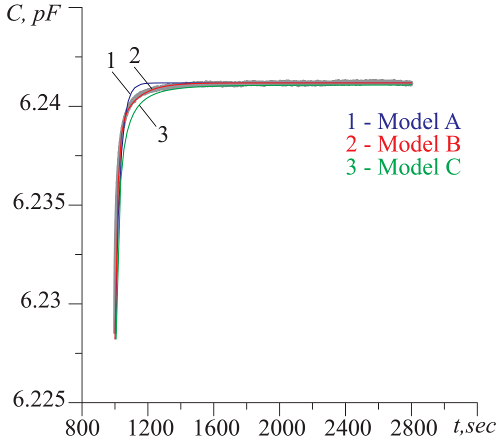

Fig. 3. Zoom of the experimental 'charging' transient of Fig. 2 (black line) and its fitting obtained with Models A, B and C.

dielectric and the increase of the effective voltage according to (7). Therefore, the capacitance would grow beyond the level shown by the dashed line.

The fitting of the experimental $C(t)$ curve obtained using Model B with two time constants is also shown in fig. 2. The fitting method is the following: the charge as a function of time is substituted into eq. (18) to obtain the displacement $x(t)$ caused by this charge and the capacitance (17) is calculated. The parameters in (12) were varied in order to obtain a good agreement with experimental data.

Figure 3 compares the fitting of the charging section of fig. 2 by Models A, B and C, with Model B being the most accurate for this case. We have tested a number of devices that exhibit very different charging constants and two representative sets of fitting parameters for Model B are summarised in table I. Results displayed in figs. 2 and 3 correspond to device 1.

Figure 4 gives a fitting for another device that is also prone to charging, but with a characteristic charging time very large when compared to devices 1 and 2. In this case, though both Model B and Model C can be used for fitting the curve, Model C is the most accurate. Since different types of devices may be described by different models, we will obtain a discrete time system and present numerical simulation for all models in order to ensure the effectiveness of the method.

III. DISCRETE-TIME MODEL

A. Position of the MEMS device

For the self-consistent electromechanical model given by eqs. (1), (7), (16) and one of (10)-(11), (12)-(13) or (14)-(15) we can obtain a discrete-time map describing the evolution of the device under our control method (16) between two consecutive sampling events. The discrete-time system later will be used for theoretical analysis and numerical simulations.

The selection of the control voltage is determined by the current capacitance value, or, according to (17), by the current position $x(t)$. We consider a sequence of discrete values of the position $x_n = x(nT_s)$ and the dielectric charge $Q_n = Q_d(nTs)$ and introduce them into the system.

For the mass-spring-damper equation (1), it is assumed that the sampling time T_s is much larger than the characteristic decay time of eigen-oscillations. Under this condition, which is generally the case, we can consider the sampled position x_n as the steady-state position of the device (1) under the external

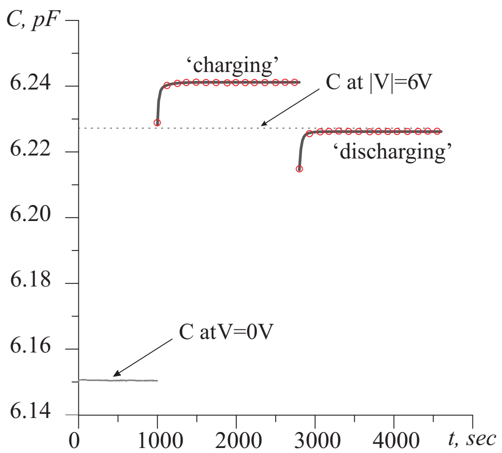

Fig. 2. Experimental capacitance transient (gray line) and its fitting obtained with Model B (red line). Fitting parameters are given in table I.

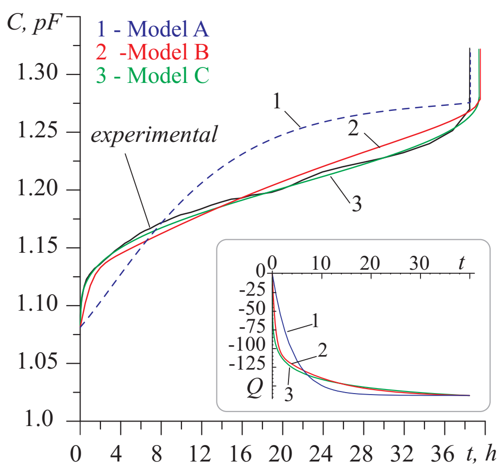

Fig. 4. Experimental capacitance transient (black line) and its fitting obtained with Models A, B and C. The insert shows the dependence of the dielectric charge with time for all these models.

net force $kx - F_{el}$, being F_{el} given by (7). Then, we can find x_n from the following equation

$$kx_n = \frac{C_n^2(V - Q_n/C_d)^2}{2\varepsilon_0 A} \tag{18}$$

In order to simplify, let us introduce the following variables

$$\begin{aligned} y_n &= x_n/g\,, \qquad \gamma = \frac{C_{g,0}}{C_d}\,, \\ \beta &= \frac{C_{g,0}^2}{2\varepsilon_0 A\,k\,g}\,, \quad V_{Q_n} = V - Q_n/C_d \end{aligned} \tag{19}$$

and write (18) in the form of the following polynomial

$$y_n(1 - y_n + \gamma)^2 - \beta V_{Q_n}^2 = 0 \tag{20}$$

After solving (20) and returning to the variable x_n, we obtain the position of the MEMS $\mathcal{X}(V, Q)$ as a function of the applied voltage and dielectric charge. The solution and analysis of the polynomial (20) is given in Appendix A. With the position sequence $\mathcal{X}_n(V, Q)$ obtained, we now proceed to the equations that describe the dielectric charging dynamics to complete the discrete-time model.

B. Charging and Discharging Dynamics

To obtain the equations for the dielectric charge dynamics, we define the decision bit sequence $b_n \in B = \{0, 1\}$ as

$$b_n = \frac{1}{2}(1 + sgn(C_{th} - C_n)) \tag{21}$$

For simplicity and in order to obtain the analogy with our experiments, we will obtain the discrete-time equations of the charging and discharging models for only negative charge. Since the total charge is a superposition and the equations for positive and negative charges have the same form, it is easy to extend the resulting iterative equations to the case of both charges. For negative charge only, $Q_d = Q_d^n$ and let us omit the upper index n in all subsequent formulas.

In order to put Model A into sampled form, we write eq. (10) using the condition $Q_0 = Q(t_0)$ at arbitrary $t_0 > 0$

$$Q_d = \begin{cases} Q_{max} + (Q_0 - Q_{max})e^{-(t-t_0)/\tau_C}\,, & V > 0 \\ Q_0 e^{-(t-t_0)/\tau_D}\,, & V < 0 \end{cases} \tag{22}$$

Now, each sampling event corresponds to the substitution into the equation of the following expressions: $t - t_0 = T_s$ and $Q_0 = Q_n$. At the next sampling time $(n+1)T_s$, the charge is found through the following discrete-time equations

$$Q_{n+1} = \begin{cases} Q_n\alpha_C + Q_{max}(1 - \alpha_C) & V > 0 \\ Q_n\alpha_D & V < 0 \end{cases} \tag{23}$$

where $\alpha_C = e^{-T_s/\tau_C}$ and $\alpha_D = e^{-T_s/\tau_D}$. With b_n defined, one can rewrite (23) in a more compact form as

$$\begin{aligned} Q_{n+1} &= \alpha_D \left(\frac{\alpha_C}{\alpha_D}\right)^{b_n} Q_n + Q_{max}(1 - \alpha_C)b_n = \\ &= \Theta_A(Q_{max}, \alpha_C, \alpha_D; Q_n, b_n) \end{aligned} \tag{24}$$

where we denoted the right part of the map shortly as $\Theta_A(\mathbf{P}_A; Q, b)$, a function of the set of parameters $\mathbf{P}_A = \{Q_{max}, \alpha_C, \alpha_D\}$ and the variables Q and b.

Model B can be presented as a superposition of exponentials in the form (24). We define α_{Ci} and α_{Di} in the same way as for the previous case, the saturation levels $Q_{max,i} = \zeta_i Q_{max}$. The auxiliary variables $Q^{(i)}$ allow one to find the total charge. At the charging stage, $V > 0$

$$\begin{aligned} Q_{n+1}^{(i)} &= Q_n^{(i)}\alpha_{Ci} + \zeta_i Q_{max}(1 - \alpha_{Ci}) \\ Q_{n+1} &= \sum_i Q_{n+1}^{(i)} \end{aligned} \tag{25}$$

At the discharging stage, $V < 0$

$$\begin{aligned} Q_{n+1}^{(i)} &= Q_n^{(i)}\alpha_{Di} \\ Q_{n+1} &= \sum_i Q_{n+1}^{(i)} \end{aligned} \tag{26}$$

Summarising, the compact form of Model B is

$$Q_{n+1} = \sum_i \Theta_A(\mathbf{P}_{Ai}; Q_n^{(i)}, b_n) = \Theta_B(\mathbf{P}_B; Q_n, b_n) \tag{27}$$

which is a superposition of the functions Θ_A with the appropriate sets of parameters $P_{Ai} = \{\zeta_i Q_{max}, \alpha_{Ci}, \alpha_{Di}\}$ and variables $Q_n^{(i)}$ and b. We denote this superposition in the right part of the equation as the function $\Theta_B(\mathbf{P}_B; Q, b)$.

Model C involves the non linear expression for time t^β and, as a consequence, the rate of change of the stretched exponential process changes with time. Thus, a simple and linear expression similar to (24) cannot be found for this model. Instead, we propose the following iterative algorithm: while the decision bit is $b_n = 1$ and the dielectric is charging, the next value of charge is calculated using the following law

$$\begin{aligned} t_{n+1} &= T_s + \tau_C(-\ln[1 - Q_n/Q_{max}])^{1/\beta_C}\,, \\ Q_{n+1} &= Q_{max}(1 - \exp[-(t_{n+1}/\tau_C)^{\beta_C}]) \end{aligned} \tag{28}$$

However, when $b_n = 0$ and one switches to discharging, we find the time instant t^* at the discharging curve $Q_D(t)$ such that $Q_D(t^*) = Q_n$ and take the next iteration using the discharging law

$$\begin{aligned} t_{n+1} &= T_s + \tau_D(-\ln[Q_n/Q_{max}])^{1/\beta_D}\,, \\ Q_{n+1} &= Q_{max}\exp[-(t_{n+1}/\tau_D)^{\beta_D}] \end{aligned} \tag{29}$$

The latter equation can be written in a compact form using the decision bit b_n

$$\begin{aligned} t_{n+1} &= T_s + \tau_D(\tau_C/\tau_D)^{b_n} \times \\ &\quad \times (-\ln[b_n + (-1)^{b_n} Q_n/Q_{max}])^{1/[\beta_D(\beta_C/\beta_D)^{b_n}]}\,, \\ Q_{n+1} &= Q_{max}(b_n + (-1)^{b_n} \times \\ &\quad \times \exp[-(t_{n+1}/\tau)^{\beta_D(\beta_C/\beta_D)^{b_n}}]) = \Theta_C(\mathbf{P}_C; Q_n, b_n) \end{aligned} \tag{30}$$

where the set of parameters for the stretched exponential is denoted as $\mathbf{P}_C = \{Q_{max}, \tau_C, \tau_D, \beta_C, \beta_D\}$. Note that in the discrete-time equation (30) the time t_n is introduced only for a simpler representation. Note also that in all models $\Theta_C(\mathbf{P}, Q, b)$ is a function of only the dielectric charge at the previous sampling time and the decision bit.

Summarizing all of the above, expressions (21) and one of (24), (27) and (30) define a map

$$\mathbb{R} \times \mathcal{B} \to \mathbb{R} \times \mathcal{B}$$

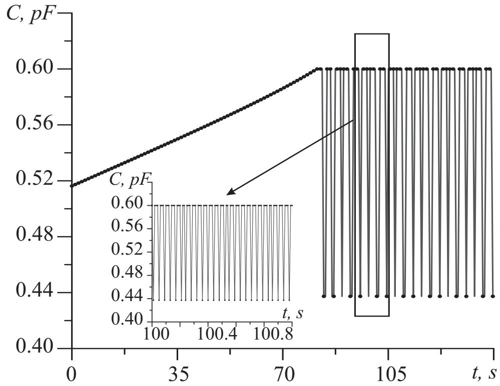

Fig. 5. Total capacitance C_{tot} as a function of time obtained as a solution of ODEs (1), (7) and (10) (solid line) and the same capacitance as a solution of the iterative map (31) (circles) when the control mechanism (16) is being applied. Parameters are taken from Table II and $\tau_C = \tau_D = 60s$.

for the state vector $\{Q, b\}$. In this map, $\mathcal{B}$ is $\{0, 1\}$ and the evolution operator is

$$T(Q, b) = \begin{pmatrix} \Theta(\mathbf{P}; Q, B) \\ \frac{1}{2}\left[1 + sgn\left(C_{th} - \frac{C_{g,0}}{1+\gamma-\mathcal{X}(V,Q)/g}\right)\right] \end{pmatrix} \quad (31)$$

where $\mathcal{X}(V, Q)$ is defined in (39) (see Appendix A) and $\Theta(\mathbf{P}; Q, B)$ is one of the functions $\Theta_{A,B,C}(\mathbf{P}, Q, b)$, depending on the charging model used.

Let us note that the map above must be established between $\mathbb{R} \times \mathcal{B} \to \mathbb{R} \times \mathcal{B}$ (and not simply between $\mathbb{R} \to \mathbb{R}$) because the rest position of the device depends on the applied voltage, and this voltage depends on the previously obtained bit. Key properties of the map (31) are given in Appendix B.

IV. Simulation Results

Using the map (31) obtained in the previous section, we carried out a large set of discrete-time simulations in order to demonstrate that the proposed method is able to keep the parasitic charge under control, avoiding undesired effects such

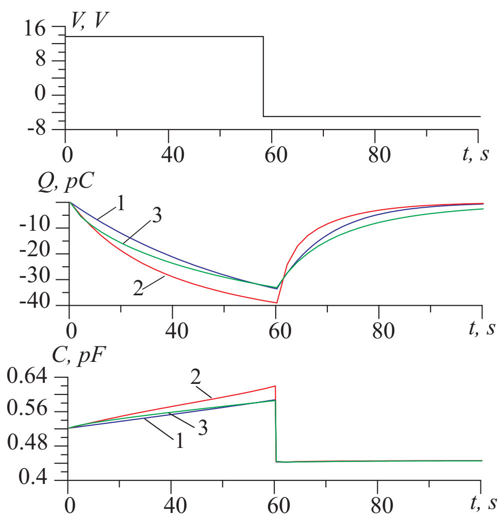

Fig. 6. Total capacitance and dielectric charge simulation transients resulting from an applied voltage sequence composed by positive $13.5V$ and negative $-5.5V$. Lines 1, 2 and 3 correspond to Models A, B and C respectively.

TABLE II
Parameter Values Used in the Simulations

Parameter	Value
A	$100 \times 500\,\mu m^2$
k	335 N/m
g	$1\,\mu m$
d	85 nm
T_s	10 ms

as time drifts or device collapse after large working periods. In experiments we have tested a number of devices with different parameters and charging/discharging characteristics. For numerical simulations we introduce a generic device whose parameters are listed in Table II. At the same time, we varied the parameters that are related to the algorithm (V_{ch}, V_{dis} and C_{th}) and to the charge dynamics (for instance, Q_{max} and the charging constants) over a wide range trying to keep them similar to our experimental devices.

Typically in simulations we use charging constants that have the order of minutes/tens of seconds, although in experiments we often observed larger constants of minutes/hours. However, since $T_s \ll \tau_{C,D}$, we may allow this simplification: if the algorithm is effective with such fast charging/discharging, it will be effective with slower processes as well.

First, we note the correspondence between the system formulated in terms of ODEs (1), (7) and (10) and the iterative map (31) obtained in the previous section. The correspondence must be very precise: all equations are solved analytically, and the only assumption made was that all time derivatives are zero. The latter is valid if the sampling time T_s is large enough. After the time $\tau_0 \sim 2m/b$ all eigen oscillations of the MEMS will decay; in our case $\tau_0 \sim 10^{-4}$ and $T_s \sim 10^{-2}$.

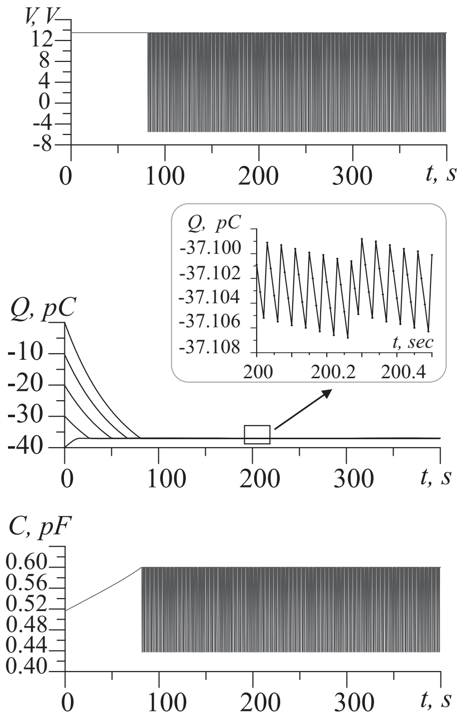

Fig. 7. Simulated capacitance and dielectric charge transients applying the charge control method. The charging model used is Model A.

Fig. 5 shows a good correspondence between the controlled capacitance $C(t)$ obtained as a solution of the ODEs and from the map.

The default value of Q_{max} used in this section is -50 pC. This may cause up to -2.4 V of the voltage shift (8) for the generic device, whose pull-in voltage is $V_{PI,d} = 15.45$ V. We also selected the value of $V_{ch} = 13.5$ V in such way that when the dielectric is fully charged (with Q_{max}), the effective total voltage will exceeds the pull-in value and device goes into the ON state.

To illustrate the working principle of the charge control method, and also to validate the response of the proposed iterative map, Fig. 6 shows a simulation with two time intervals corresponding to states that can be achieved during the application of the control method. A positive voltage is first applied and the parasitic charge and the capacitance slowly grow. Note that if the voltage is applied for a longer time, the additional electrostatic force due to the dielectric charge leads the device to pull-in. Next, after 60 s, a negative voltage is applied and thus charge is removed from the dielectric and the capacitance returns to a value closer to the initial. In this figure, the dynamics for charging models A, B and C are shown.

Figure 7 shows the simulation results when the charge control method is implemented with the same voltage values as in Fig. 6, with $C_{th} = 0.6\,pF$ and using Model A. In this case, both the capacitance and the parasitic charge increase when the positive voltage is applied until C_{th} is reached. At this moment, the control method applies the negative voltage, forcing the capacitance to decrease due to the jump to a new steady-state position and due to charge removal. At the next sampling time, the capacitance is under the threshold value, so the positive voltage is reapplied and the cycle restarts. It is shown that this method allows one to maintain the parasitic charge under control, avoiding device collapse even after long periods of time. Note that the device capacitance is kept predominantly under C_{th}, but with oscillations of about $0.15\,pF$. However, this amplitude decreases for increasing values of the sampling frequency.

The algorithm is applicable to all charging models proposed in Sec. II. Control waveforms for other models, B and C have the same form and instead of presenting them as a plot, we summarise the result in table III. For each model with particular parameters listed in the table, we give the maximal and minimal values of Q_d and C_{tot} in a steady-state control cycle of the algorithm. Despite minor variations, the algorithm is capable of fixing the capacitance at the target level for all models.

The parameters in the first three cases in the table are selected to model the charging and discharging patterns from fig. 6. However, Model B(2) presents a sample of numerical simulations at the parameters of the charging/discharging dynamics that are 'inspired' by the fitting results discussed in Section II (device 2 from table I). In this case, the variation of the capacitance is about 0.07 pF, which is smaller than in the previous examples.

The bit stream sequence b_n corresponding to the "steady-state" phase of Fig. 7 is strongly regular, and mostly consists of series of '1' separated by a single '0'. In order to understand this, we must take into account that each time we apply a positive voltage, the rest position drifts due to the dielectric charge accumulation until C_{th} is reached. Applying a negative voltage after that immediately decreases the capacitance below the target level. (There is an asymmetry in actuation, see eq. (7), such that electrostatic force is always different in the presence of the dielectric charge even if $V_{ch} = |V_{dis}|$.) After that a new cycle of charging starts. Therefore the system tends to oscillate around the target capacitance until the drift is too large, forcing then a change in the bit sequence.

It is important to note that the algorithm is insensitive to initial conditions. The plot of the dielectric charge as a function of time $Q_d(t)$ from fig. 7 starts from various initial conditions and, as one can see, the same steady-state level of Q_d is reached and the same b_n is displayed in all cases.

In order to show that the algorithm is capable of fixing the target charge, in fig. 8 we compare the dielectric charge fixed by the control method Q_d with the "desired" level of charge, calculated analytically through eq. (40), as a function of the threshold capacitance C_{th}. As is seen from the figure, except for small values of C_{th}, the method precisely fixes the charge. The area where the method fixes Q_d different from the target level depends on the ratio τ_D/τ_C.

We have also studied the behaviour of the system over a wide range of control parameters. To this effect, planes of parameters $(\tau_D/\tau_C, C_{th})$ for Model A have been obtained from numerical simulations. In the plane shown in fig. 9, the same range of C_{th} as in fig. 8 and one reasonable range of

TABLE III
ALGORITHM PERFORMANCE FOR MODELS A, B AND C

Model A: $\tau_C = \tau_D = 60$ s, $C_{th} = 0.6$ pF ($Q_{th} = -37.1048$ pC)
$Q_{max} = -50$ pC, $V_{ch} = 13.5$ V, $V_{dis} = -5.5$ V

Q_{min}, pC	Q_{max}, pC	C at V_{ch}, pF	C at V_{dis}, pF
-37.1069	-37.0987	0.600013	0.437307

Model B (1): $\tau_{C1} = \tau_{D1} = 60$ s, $\tau_{C2} = \tau_{D2} = 15$ s
$\zeta_1 = 0.6$, $\zeta_2 = 0.4$, $C_{th} = 0.6$ pF ($Q_{th} = -37.1048$ pC)
$Q_{max} = -50$ pC, $V_{ch} = 13.5$ V, $V_{dis} = -5.5$ V

Q_{min}, pC	Q_{max}, pC	C at V_{ch}, pF	C at V_{dis}, pF
-37.1095	-37.0918	0.600029	0.437308

Model C: $\tau_C = \tau_D = 60$ s, $\beta = 0.75$
$C_{th} = 0.60$ pF ($Q_{th} = -37.1048$ pC)
$Q_{max} = -50$ pC, $V_{ch} = 13.5$ V, $V_{dis} = -5.5$ V

Q_{min}, pC	Q_{max}, pC	C at V_{ch}, pF	C at V_{dis}, pF
-37.1062	-37.0979	6.00009	0.437307

Model B (2): $\tau_{C1} = \tau_{D1} = 230$ s, $\tau_{C2} = \tau_{D2} = 10$ s
$\zeta_1 = 0.2$, $\zeta_2 = 0.8$, $C_{th} = 0.55$ pF ($Q_{th} = -32.59538$ pC)
$Q_{max} = -50$ pC, $V_{ch} = 13$ V, $V_{dis} = -13$ V

Q_{min}, pC	Q_{max}, pC	C at V_{ch}, pF	C at V_{dis}, pF
-32.6074	-32.5704	0.550025	0.48177

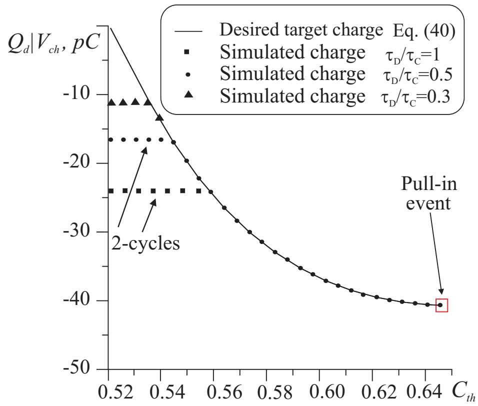

Fig. 8. Desired dielectric charge as a function of C_{th} (solid line) and charge fixed by the algorithm at $\tau_D/\tau_C = 1$ (squares), 0.5 (circles) and 0.3 (triangles). The minimal value of C_{th} corresponds to C_{tot} at $V = V_{ch}$, while the maximum corresponds the critical value at which the device is pulled in.

τ_D/τ_C are considered. In all these cases, the control algorithm fixes the desired dielectric charge and prevents the device from pull-in. We only note that in the region marked as 'controlled (2)' the charge that is fixed is larger than desired. See a detailed discussion on planes and comparison with theory in Appendix B.

Finally, we discuss the influence of V_{ch} and V_{dis} on the performance of the algorithm. These parameters affect the saturation level Q_{max} and charging/discharging constants. Properly selected voltages can also decrease the oscillations of the capacitance. From the plane in fig. 9, it is clear that the algorithm is effective for a range of C_{th}, τ_D/τ_C and Q_{max}, and in most cases minor variations of voltage values are not crucial. The only condition we impose is that there must be charging of the dielectric at V_{ch} (note that there is always discharging at V_{dis} even if $V_{dis} = 0$). Based on our own experiments, we can conclude that charging is often the case for V_{ch} that are below pull-in $V_{PI,d}$. We do not impose any specific condition for V_{dis}, however, again from our experiments and the literature [11], it is known that if

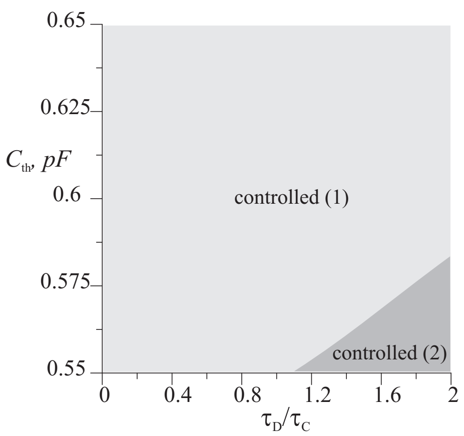

Fig. 9. Plane of parameters $(\tau_D/\tau_C, C_{th})$ showing the effectiveness of the control method for Model A at $Q_{max} = -50$ pC. For all values of the control parameters C_{th} and τ_D/τ_C the method fixes the dielectric charge $|Q_{d|} < |Q_{max}|$, however, the area marked as 'controlled (2)' corresponds to 2-cycles and the fixed charge is slightly larger than the desired level.

strongly affects τ_{dis} and the increase of V_{dis} decreases the area of 2-cycles in fig. 8 and fig. 9 and in general improves algorithm performance.

V. Experimental results

In order to experimentally validate the feasibility of the control method introduced and discussed in the previous sections, an extensive set of measurements with and without applying the control method to different MEMS devices has been performed. As it was commented above, we have tested several devices made with two different technologies: PolyMUMPS and a specific process of our own. All theses devices are capacitive switches-like, with silicon nitride as the dielectric material, and they exhibit radically different time constants in the charging and discharging processes.

The experimental setup is based on an Agilent E4980A precision LCR meter, which was used both to measure the MEMS capacitance and to apply the bias voltages, V_{ch} and V_{dis}, accordingly to the method. The device capacitance was sampled every 50 ms using a 1 MHz / 50 mV AC test signal.

The MEMS device chosen to illustrate the control method for the OFF state was designed and fabricated in our clean room following the process described in [34]. It is a typical bridge structure with a $100\mu m \times 500\mu m$ aluminium beam held by two anchors above a silicon nitride layer. The dielectric layer prevents short-circuiting between the movable beam and the bottom contact, i.e. the fixed plate, when the device is actuated to close. The air gap in the rest state is $1\mu m$, whereas the aluminium plate and the silicon nitride thickness are $900nm$ and $85nm$ respectively. This device can be identified as device 3 in Table I, which exhibits charging times of hours.

Fig. 10 shows the C–V characteristic of the MEMS device. Note that the curve is not symmetrical since, due to the fabrication process, some permanent charge exists. The pull-in voltage when only such permanent charge is stored in the dielectric (initial or "discharged" state) is $V_{PI}(Q_d = 0) = 15.42\,V$.

Fig. 11a shows the capacitance transients obtained by applying or not the control method. The plot marked as '1' is the capacitance transient obtained when a constant voltage $V_{ch} = 13.5\ V$ is applied to the MEMS for 55 hours. The measurement starts with an initial time lapse of 300 s, on which zero voltage is applied to set the device to its initial or 'discharged' state. After that, the measurement time line clearly exhibits two different behaviours. In the first one, which lasts until the 38^{th} hour, it is seen that the capacitance increases about $260\ fF$ due to charge accumulation. From t=38h on, the measured capacitance remains around its maximum value, since the device is closed. Note that the change in behaviour seen at $t = 38\ h$ is due to the fact that the injected charge during the previous phase produces an additional and slowly-increasing electrostatic force that leads to a pull-in event, forcing the device to collapse despite the fact that the control voltage is always under the pull-in value. This is exactly the same phenomenon previously seen in the simulations.

The plot marked as '2' in Fig. 11a shows the capacitance transient when applying the control method with $C_{th} =$

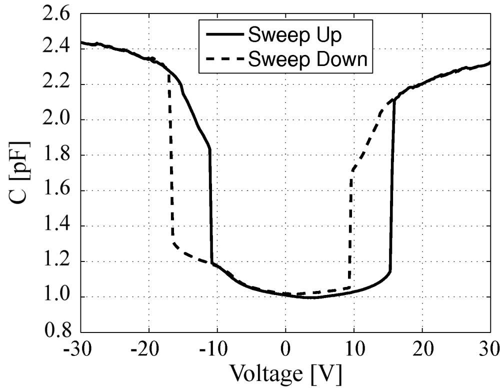

Fig. 10. Capacitance-voltage characteristic of the MEMS device.

$1.1pF$, which is in strong contrast with plot '1'. V_{ch} is applied until the capacitance reaches C_{th}. At this point, a V_{dis} pulse is applied for the first time. From then on, voltage switches to V_{ch} or V_{dis} accordingly to the value of the current capacitance samples. After the first hour some "steady-state" behaviour is reached, with capacitance values closer to C_{th} (see magnification in Fig. 11b), implying that the dielectric charge is kept under a certain value. The slight variations seen in the steady-state regime are most probably due to variations in the environmental conditions, which were not controlled during the measurement, such as humidity, which has been found to influence in great measure charge injection in dielectrics. However, this perturbation of the capacitance decays with time and the capacitance returns to its target level.

In the OFF state, the capacitance may be tuned to values up to $C_{max} = (3/2)C_{g,0}/[1 + 3/2\gamma]$. Voltage switching causes some inevitable mechanical movement, reflected as capacitance oscillations of around $30fF$ with respect to the target value. This indeed reflects the fact that even loose position control with bipolar voltages allows efficient control of the dielectric charge. However note that as follows from the model and numerical simulations, these movement can be significantly reduced by adjusting the charging and discharging voltages and the sampling time (see, for instance, simulations of Model B2 in Table III).

In order to contrast the effects of the parasitic charge stored in the dielectric layer between applying and not the charge control method in terms of charge, C–V characteristics of the MEMS device have been obtained before and after the experiments. The comparison of the C–V characteristic obtained after each measurement with the one measured with no parasitic charge (see Fig. 10) allows us to extract the shift of the pull-in voltage value. Thus assuming a sheet of charge trapped in top of the dielectric layer, the expression for the pull-in voltage is

$$V_{PI} = V_{PI}(Q_d = 0) + V_{shift} \tag{32}$$

being $V_{PI}(Q_d = 0)$ the pull-in voltage with no trapped charge and V_{shift} the voltage shift due to the parasitic charge from eq. (8).

Fig. 12 shows the C–V measurements of the MEMS after applying several voltage stresses, as well as the "discharged" one (solid line). Note that the C–V curves always shift to the left, which is consistent with (32) taking into account that most of the time the control method is applying positive voltages, therefore leading to negative amounts of parasitic charge. Furthermore, such displacements of the C–V curves agree with previous works involving silicon nitride as dielectric [6], [20], [21]. However this behaviour may vary when other dielectric materials are used. It is also noteworthy that when the control method is applied it can be seen that V_{shift} is always less than the one obtained applying a constant positive voltage. A summary of the results found for two control experiments using different discharge voltages can be seen in Table IV. In both cases a 2-cycle bit stream (composed of chains of '10') has been obtained for the capacitance threshold applied.

TABLE IV
RESULTS OBTAINED FROM THE C–V CURVES OF FIG. 12 AND THEORETICALLY PREDICTED VALUES OF THE DIELECTRIC CHARGE

Measure type	V_{ch} $[V]$	V_{disch} $[V]$	V_{pi} $[V]$	V_{shift} $[V]$	Q_d $[pC]$
Discharged	–	–	15.419	0	0
Uncontrolled	13.5	–	12.65	-2.7	-58.57
Controlled	13.5	-3.5	14.48	-0.94	-19.79
Controlled	13.5	-5.5	15.07	-0.35	-7.31
Theoretically	13.5	-3.5	–	–	-15.1
predicted	13.5	-5.5	–	–	-7.9

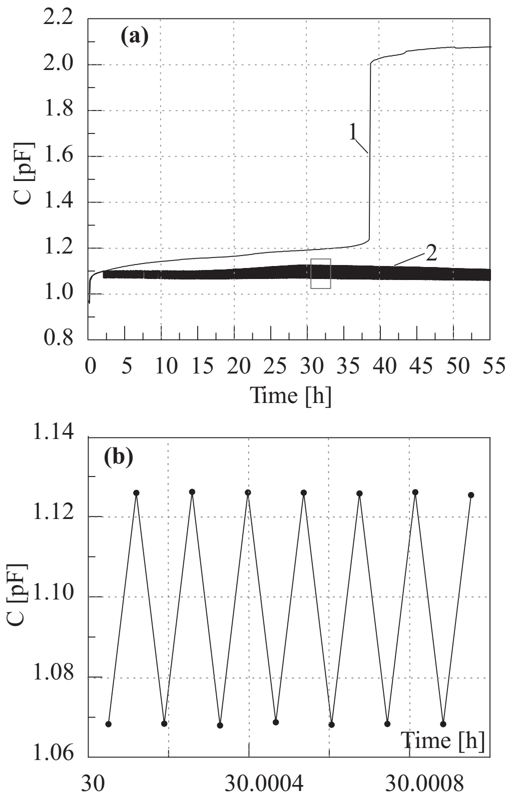

Fig. 11. (a) Plot '1': Experimental capacitance transient obtained applying a constant voltage $V_{ch} = 13.5V$, i.e. with no control method; plot '2': experimental capacitance transient obtained applying the charge control method with $V_{ch} = 13.5V$ and $V_{dis} = -5.5V$. (b) Zoom-in of the "steady-state" section of plot '2'.

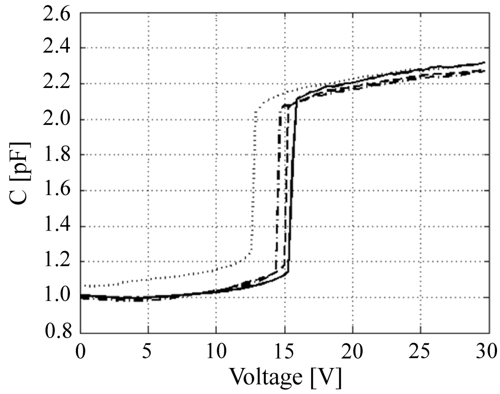

Fig. 12. Experimental C–V characteristics of the MEMS device after applying several voltage stresses: before any stress (solid line), after 55h with a constant voltage $V_{ch} = 13.5V$ (dotted line), after 55h with control using $V_{ch} = 13.5V$ and $V_{disch} = -3.5V$ (dash-dot line), after 55h with control using $V_{ch} = 13.5V$ and $V_{disch} = -5.5V$ (dashed line).

Note that V_{dis} may play an important role in the performance of the control method for a given device, since V_{shift} strongly depends on this value when 2-cycle bit streams are obtained (i.e. see fig. 8). In the case shown here, it is clearly seen that $V_{dis} = -5.5V$ works better than $V_{dis} = -3.5V$, since the resulting pull-in voltage is closer to the "discharged" one.

Furthermore, according to (32), Table IV shows values extracted from the measurements shown in Fig. 12, including and estimation of the parasitic charge fixed on each case. We also give theoretically predicted values of the dielectric charge in this table. It evidences the utility of the charge control method, as the pull-in voltage shift is strongly reduced after long actuation cycles, allowing one to maintain the effective V_{PI} within expected margins, therefore avoiding undesired long-time effects such as capacitance/position drift or device collapse.

Finally, this method can be also applied to devices in the ON state. Since for almost all devices, the C(V) characteristic is not perfectly flat beyond pull-in, it is possible to sense changes in the charge stored in the dielectric by measuring changes in the capacitance of the device beyond the pull-in. Some preliminary results can be observed in fig. 13 for a PolyMUMPS device consisting on a moveable electrode of $360\mu m \times 360\mu m$, held by four suspension arms in "L" over the bottom-fixed electrode, which is the doped silicon substrate. A $0.6\mu m$ silicon nitride layer is the dielectric. The air gap in the rest state is $2\mu m$. This device can be identified as device 1 in Table I and exhibits charging times of a few minutes. The C(V) characteristic of the device actuated with this control method remains closer to the one of the discharged device than in the case when the device is simply actuated with a constant voltage.

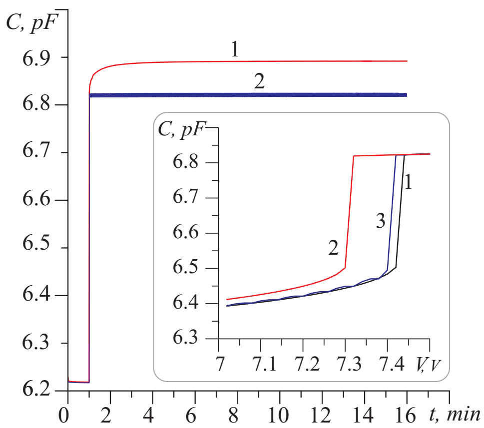

Fig. 13. Experimental capacitance transients obtained applying a constant voltage $V_{ch} = 8.5V$ (line 1), and applying the control method with $V_{ch} = 8.5V$ and $V_{disch} = -8.5V$ (line 2). The insert shows a magnified part of the C–V characteristics similar to the one presented in fig. 12; line 1: discharged device, line 2: after 15 min charging and line 3: after 15 min with control.

VI. Conclusions

A new control method for enhanced reliability and robustness in capacitive MEMS devices has been proposed and experimentally verified. The method involves real-time capacitance sampling and actuation through bipolar pulses of constant magnitude, in order to keep dielectric charge under control. It has been shown that a loose position control may provide a good control of the charge in the dielectric. The scheme has been successfully validated in MEMS devices that suffer from dielectric charging.

We have also proposed a simple and effective model that explains the mechanical behaviour of the device, shows that the dielectric charge can be fixed and estimates the parameters with which the control method will work well.

The experiments carried out are in good agreement with the simulations of the proposed models: both show that an almost constant charge is maintained in the dielectric.

Appendix A: The solution of the Polynomial

The standard way to analyse (20) is to reduce it to the canonical form

$$\xi_n^3 + p\xi_n + q = 0 \tag{33}$$

by introducing the variable y_n and the parameters p, q

$$\begin{gathered} y_n = \xi_n + 2(1+\gamma)/3, \\ p = -\frac{1}{3}(1+\gamma)^2, \quad q = \frac{2}{27}(1+\gamma)^3 - V_{Q_n}^2\beta \end{gathered} \tag{34}$$

Now, the polynomial (33) can be solved by using Cardano's method. Introducing the auxiliary parameters

$$\begin{gathered} D = (p/3)^3 + (q/2)^2, \\ \alpha_p = \sqrt[3]{-q/2 + \sqrt{D}}, \quad \beta_p = \sqrt[3]{-q/2 - \sqrt{D}} \end{gathered} \tag{35}$$

we obtain the solutions of the reduced polynomial (33) as

$$\begin{aligned} \xi_{n,1} &= \alpha_p + \beta_p, \\ \xi_{n,3} &= -\frac{\alpha_p + \beta_p}{2} - i\sqrt{3}\frac{\alpha_p - \beta_p}{2}, \\ \xi_{n,2} &= -\frac{\alpha_p + \beta_p}{2} + i\sqrt{3}\frac{\alpha_p - \beta_p}{2} \end{aligned} \tag{36}$$

In the case $V_n < V_{PI}$ (V_n below pull-in voltage), the discriminant in (35) is $D < 0$, and, therefore, α_p and β_p

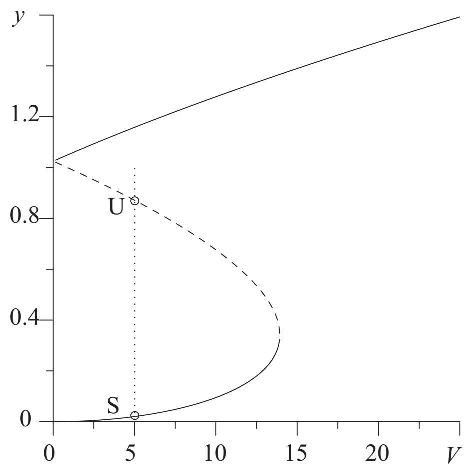

Fig. 14. Roots of the polynomial as a function of the applied voltage: the branch of stable roots (S) is shown by the solid lines while the unstable (U) by the dashed one. The insert shows the potential well $W(x)$ (solid line) and the derivative of the function $f(x)$ (dashed line).

are complex conjugates. In general, there exist three pairs of α_p and β_p and those of them must be chosen which fulfil the condition $\alpha_p \cdot \beta_p = -p/3$ (at least one such pair exists).

The original position is restored as

$$x_{n,i} = y_{n,i} \cdot g = g(\xi_{n,i} + 2(1+\gamma)/3)\,, \quad i = 1,2,3 \tag{37}$$

where

$$\begin{aligned} \xi_{n,1} = 2\,\mathrm{Re}\,\alpha_p\,, \quad \xi_{n,3} = -\mathrm{Re}\,\alpha_p + \sqrt{3}\mathrm{Im}\,\alpha_p\,, \\ \xi_{n,2} = -\mathrm{Re}\,\alpha_p - \sqrt{3}\mathrm{Im}\,\alpha_p \end{aligned} \tag{38}$$

Formally, it can easily be shown that in order to guarantee that the root y_n^* is stable, the derivative of the function $f(y)$ must be positive. Thus, the root that we look for is the last of the three in (38)

$$x_n = g(-\mathrm{Re}\,\alpha_p - \sqrt{3}\,\mathrm{Im}\,\alpha_p + 2(1+\gamma)/3) = \mathcal{X}(V, Q_n) \tag{39}$$

where we define the function $\mathcal{X}(V,Q)$ as the solution to the polynomial for a given applied voltage and dielectric charge.

The behaviour of the roots of (20) agrees with well-known facts. As an example, for $V < V_{PI}$ there are three roots $y_{n,i}$ with one of them lying in the non-physical region below the bottom electrode ($y_n > 1$), and a pair of a stable root and an unstable root within the gap ($y_n < 1$). For $V = V_{PI}$ the stable and the unstable roots join and disappear, with only one stable position under the bottom electrode left; this corresponds to collapse of the device due to the pull-in effect. This effect is clearly seen in Fig. 14, which shows the roots calculated from (37) as a function of applied voltage.

Appendix B: Properties of the Map

Let us first consider our major case when the device is OFF and we expect that the method will prevent it from pull-in. So far we have introduced the target capacitance by eq. (16). However, we may also speak in terms of the target charge Q_{th}. Indeed, (18) allows one to link these two parameters: the presence of any non-zero Q_d causes the drift of capacitance and there is such Q_{th}, accumulating which the total capacitance is equal to C_{th}.

From the definition of the total capacitance (5) using the net force balance (18) we obtain that if at a given time the measured capacitance is C and the applied voltage is V, the accumulated charge is

$$Q = C_d \left(V - \sqrt{\frac{1+\gamma - C_{g,0}/C}{\beta} \frac{C_{g,0}^2}{C^2}} \right) \tag{40}$$

This way, by substituting V by V_{ch} and C by C_{th}, we may find the charge, Q_{th}, associated to the charging voltage, V_{ch}, assuming that the control will locate the capacitance of the device near C_{th}.

In the same manner, the 'collapse' charge Q_c is the amount of charge required to put the device in the ON state (pull in)

$$\begin{aligned} Q_c = C_d(V - V_{PI,d}) = \\ C_d \left[V - \sqrt{\frac{8kg^3}{27\varepsilon_0\varepsilon_g A} \left(1 + \frac{d}{\varepsilon_d g}\right)^3} \right] \end{aligned} \tag{41}$$

Let us return to the map and discuss first the case of Model A and function Θ_A in (31). With Q_{th} introduced, we conclude that it can be presented as a piecewise contractive map with the partition $\{Q_k\}_{k=1}^2$ of the state space $Q \in \mathbb{R}$ given as follows : $Q_1 = \{Q : Q \le Q_{th}\}$ and $Q_2 = \{Q : Q > Q_{th}\}$. In each partition, a map is define in the form: $G(Q) := G_k(Q) = \alpha_C Q + (1-\alpha_C)Q_k^*$ with the fixed points $Q_1^* = Q_{max}$ and $Q_2^* = 0$. Model B is a more general case of a piecewise contraction in the plane. Maps written in this form are considered in the work [35], which states that piecewise contractions of this form are *asymptotically periodic*, i.e. their steady-state solutions are *stable cycles*.

Thus, the maps are always stable. However, certain conditions appear due to physical properties of the device, namely, mechanical instability and pull-in, that do not implicitly appear in the map. Returning to the collapse charge, the condition $Q_d \ge Q_c$ defines the appearance of mechanical instability in the system and, from the standpoint of the algorithm effectiveness, it separates the case where the algorithm can control the charge and prevent the device from going into the ON state during the charging phase (V_{ch} applied) and where the algorithm cannot (note that even in this case the charge will be fixed to a certain value).

For a given N-periodic sequence $\{b_n\}_{n=1}^N$, let us find the solution of the map that defines an N-periodic sequence of $\{Q_n\}_{n=1}^N$. For simplicity, we write it for Model A. Let us introduce the parameters $\nu = \alpha_C/\alpha_D$, $\mu = Q_{max}(1-\alpha_C)$ and the sum

$$S_p^q = \sum_{j=p}^{q} b_{n+j} \tag{42}$$

for $p \le q$. (For the terms in this sum with the index $n+j > N$, the fact that the sequence is periodic must be used.) The kth iteration of the map is

$$Q_{n+k} = \alpha_D^k \nu^{S_0^{k-1}} Q_n - \mu \sum_{j=1}^{k-1} \alpha_D^{k-j} \nu^{S_j^{k-1}} b_{n+j-1} - \mu b_{n+k-1} \tag{43}$$

Since the sequence $\{b_n\}$ is periodic [35], $Q_n = Q_{n+N}$. Using N instead of k and $S^N = S_0^{N-1}$ as the sum of all b_n in the sequence, we write that

$$Q_n = \frac{-\mu}{1-\alpha_D^N \nu^{S^N}} \left(b_{n+N-1} + \sum_{j=1}^{N-1} \alpha_D^{N-j} \nu^{S_j^{N-1}} b_{n+j-1} \right) \tag{44}$$

Thus, expression (44) generates Q_n for any given control sequence.

Note that the algorithm allows only sequences where subsequent discharging events are not possible due to asymmetry in electrostatic force: applying discharging voltage V_{dis} will cause the jump of the position below the target level and, consequently, a sharp change in the total capacitance such that $C_{tot} < C_{th}$. This, in its turn, leads to applying the charging voltage V_{ch} in the next sampling event.

The 2-cycle, a particular case of (44), is a special solution that corresponds to the control sequence $B_2 = (1, 0)$ (one charging and one discharging event) and is defined as

$$\hat{Q}_1 = -\frac{\alpha_D \mu}{(1-\beta)}, \qquad \hat{Q}_2 = -\frac{\mu}{(1-\beta)} \tag{45}$$

where we denoted $\beta = \alpha_C \alpha_D$. The 2-cycle corresponds to the minimal amount of charge in the dielectric that can be fixed by the algorithm, and we can impose the basic condition when the algorithm will be capable of stabilizing the system below pull-in, namely, $|\hat{Q}_2| < |Q_c|$, providing the following boundary condition

$$-\frac{\mu}{(1-\beta)} = Q_c \tag{46}$$

The other condition defines whether the algorithm is capable of fixing the exact target charge introduced by (40)

$$-\frac{\alpha_D \mu}{(1-\beta)} = Q_{th} \tag{47}$$

Due to parameter selection the target charge can be less than the one given by the 2-cycle, and the algorithm will fix the charge that corresponds to the 2-cycle but not the one of the target. The above solutions, the 2-cycle expression and these basic conditions can be obviously to Model B. As far as Model C concerns, it displays similar properties since it is also a contractive map.

The conditions (46) and (47) allow us to plot planes of control parameters analytically and study the behaviour of the system varying all system parameters. As an example, let us consider the plane $(\tau_D/\tau_C, C_{th})$. C_{th} is controlled directly by selecting the desired level of the capacitance. The ratio τ_D/τ_C can be seen as a property of the dielectric material or and may be controlled by the voltages, and we are interested to see the change in the dynamics over a wide range of these parameters.

An example of the plane is shown in fig. 15. We have selected the parameters we had already used in Sec. IV with numerical simulations: $V_{ch} = 13.5$ V and $V_{dis} = -5.5$ V and $Q_{max} = -50$ pC (recall that this charge in enough to pull in the device). The two lines, 1a and 2a, correspond to the conditions (46) and (47). The red line 1a divides the plane into two areas where the charge is controlled (on the left) and

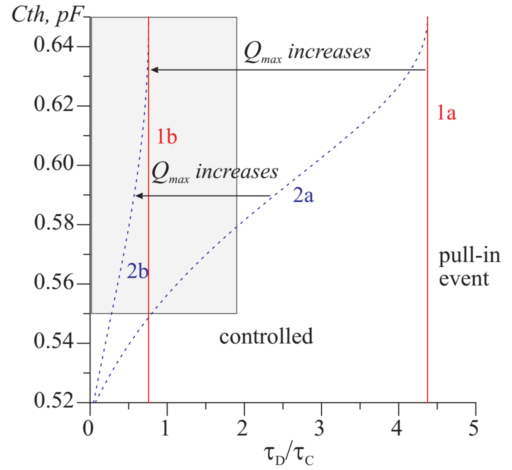

Fig. 15. Analytically calculated plane of parameters $(\tau_D/\tau_C, C_{th})$ showing the effectiveness of the control method for Model A. $V_{ch} = 13.5$ V and $V_{dis} = -5.5$ V. The two lines, 1a and 2a, correspond to the conditions (46) and (47). The red solid line 1a divides the plane into two areas, where the charge is controlled and where is not (pull-in event). The blue dashed line 2a bounds a specific area of the controlled charge — the area of 2-cycles. The evolution of the above areas with an increase of Q_{max} are shown by the arrows and the set of lines 1b and 2b. ($Q_{max} = -100$ pC versus $Q_{max} = -50$ pC). The numerically simulated plane in fig. 9 corresponds to the highlighted piece of this plane with relevant line marked as 2a, i.e. at $Q_{max} = -50$ pC.

where is not or pull-in event (on the right). The blue line 2a defines a specific area located below the line — the area of 2-cycles. If Q_{max} increases (see, for instance, the set of lines 1b and 2b for $Q_{max} = -100$ pC), the boundary lines move to the left, diminishing the area of control, while if Q_{max} decreases, the lines move to the right, expanding this area. Thus, if the algorithm fixes the charge, it will be the target value (40) or the charge of the 2-cycle (45). Note that the numerically simulated plane 9 corresponds to a highlighted piece of this plane with relevant line marked as 2a, i.e. at $Q_{max} = -50$ pC, which fully agrees with the theory.

The same plane but for $V_{ch} = |V_{dis}| = 12$ V is shown in fig. 16. Note that we had to proportionally increase Q_{max}

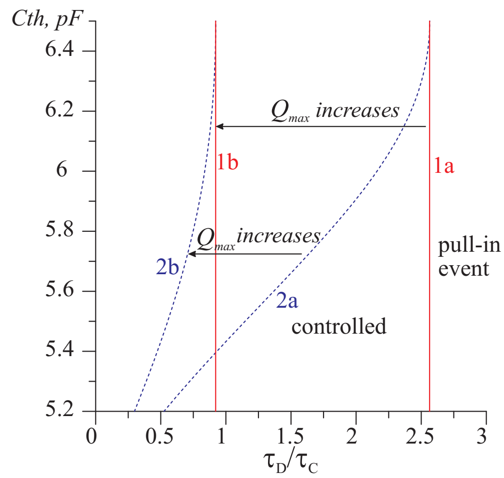

Fig. 16. Analytically calculated plane of parameters $(\tau_D/\tau_C, C_{th})$, as in fig. 15, but for $V_{ch} = -V_{dis} = 12$ V, $Q_{max} = -100$ pC (lines 1a and 2a) and $Q_{max} = -150$ pC (lines 1b and 2b).

since at $V_{ch} = 12$ and at the old value of $Q_{max} = 50$ pC we will be unable to see pull-in and we would see that for all this range of C_{th} and τ_D/τ_C the charge is controlled at the target level. The variation of the applied charging and discharging voltages changes Q_{th} and Q_c given by (40) and (41) and the ratio τ_D/t_C. Therefore, it affects the areas separated by the lines in the plane. In this particular example, when V_{ch} was selected smaller than in the plane 15, the decrease of V_{ch} expands the area of the effective control of the devices.

References

[1] S. Lucuszyn (edt.), *Advanced RF MEMS*. Cambridge University Press, 2010.

[2] W. A. de Groot, J. R. Webster, D. Felnhofer, and E. P. Gusev, "Review of device and reliability physics of dielectrics in electrostatically driven MEMS devices," *IEEE Trans. Device Mat. Rel.*, vol. 9, pp. 190–202, 2009.

[3] J. Wibbeler, G. Pfeifer, and M. Hietschold, "Parasitic charging of dielectric surfaces in capacitive microelectromechanical systems (MEMS)," *Sensors and Actuators A*, vol. 71, pp. 74–80, 1997.

[4] C. Goldsmith, J. Ehmke, A. Malczewski, B. Pillans, S. Eshelman, Z. Yao, J. Brank, and M. Eberly, "Lifetime characterization of capacitive RF MEMS switches," in *2001 IEEE MTT-S International Microwave Symposium Digest*, Phoenix, AZ, May 20–25 2001, pp. 227–230.

[5] J. R. Webster, C. W. Dyck, C. D. Nordquist, J. A. Felix, M. R. Shaneyfelt, J. R. Schwank, and J. C. Banks, "Process-induced trapping of charge in PECVD dielectrics for RF MEMS capacitive switches," in *Proc. of 43rd (2005) Annual IEEE International Reliability Physics Symposium*, 17–21 April 2005, pp. 330–336.

[6] D. Molinero, R. Comulada, and L. Castaner, "Dielectric charge measurements in capacitive microelectromechanical switches," *Applied Physics Letters*, vol. 89, p. 103506, 2006.

[7] S. M. Sze and K. K. Ng, *Physics of Semiconductor Devices. Third Edition*. Wiley, 2007.

[8] M. Razeghi, *Fundamentals of Solid State Engineering. Second Edition*. Springer, 2006.

[9] S. Melle, D. De Conto, D. Dubuc, K. Grenier, O. Vendier, J.-L. Muraro, J.-L. Cazaux, and R. Plana, "Reliability modeling of capacitive RF MEMS," *IEEE Trans. Microwave Theory Tech.*, vol. 53, pp. 3482–3488, 2005.

[10] M. Lamhamdi, P. Pons, U. Zaghloul, L. Boudou, F. Coccetti, J. Guastavino, Y. Segui, G. Papaioannou, and R. Plana, "Voltage and temperature effect on dielectric charging for rf-mems capacitive switches reliability investigation," *Microelectronics Reliability*, vol. 48, pp. 1248–1252, 2008.

[11] S. Kalicinski, M. Wevers, and I. De Wolf, "Charging and discharging phenomena in electrostatically-driven single-crystal-silicon MEM resonators: DC bias dependence and influence on the series resonance frequency," *Microelectronics Reliability*, vol. 48, pp. 1221–1226, 2008.

[12] G. Bahl, R. Melamud, B. Kim, S. A. Chandorkar, J. C. Salvia, M. A. Hopcroft, D. Elata, R. G. Hennessy, R. N. Candler, R. T. Howe, and T. W. Kenny, "Model and observations of dielectric charge in thermally oxidized silicon resonators," *J. Microelectromech. Syst.*, vol. 19, pp. 162–174, 2010.

[13] G. Bahl, J. C. Salvia, R. Melamud, B. Kim, R. T. Howe, and T. Kenny, "AC polarization for charge-drift elimination in resonant electrostatic MEMS and oscillators," *J. Microelectromech. Syst.*, vol. 20, pp. 355–364, 2011.

[14] X. Yuan, Z. Peng, J. C. M. Hwang, D. Forehand, and C. L. Goldsmith, "A transient SPICE model for dielectric-charging effects in RF MEMS capacitive switches," *IEEE Trans. Electron Devices*, vol. 53, pp. 2640–2648, 2006.

[15] ——, "Acceleration of dielectric charging in RF MEMS capacitive switches," *IEEE Trans. Device Mat. Rel.*, vol. 6, pp. 556–563, 2006.

[16] Z. Peng, X. Yuan, J. C. M. Hwang, D. I. Forehand, and C. L. Goldsmith, "Superposition model for dielectric charging of RF MEMS capacitive switches under bipolar control-voltage waveforms," *IEEE Trans. Microwave Theory Tech.*, vol. 55, pp. 2911–2918, 2007.

[17] D. Czaplewski, C. Dyck, H. Sumali, J. Massad, and J. Kuppers, "A soft-landing waveform for actuation of a single-pole single-throw ohmic RF MEMS switch," *J. Microelectromech. Syst.*, vol. 15, pp. 1586–1594, 2006.

[18] T. Ikehashi, T. Miyazaki, H. Yamazaki, A. Suzuki, E. Ogawa, S. Miyano, T. Saito, T. Ohguro, T. Miyagi, Y. Sugizaki, N. Otsuka, H. Shibata, and Y. Toyoshima, "An RF MEMS variable capacitor with intelligent bipolar actuation," in *IEEE International Solid-State Circuits Conference, 2008 (ISSCC 2008)*, 3-7 Feb, 2008, pp. 581–583.

[19] H. Yamazaki, T. Ikehashi, T. Ohguro, E. Ogawa, K. Kojima, K. Ishimaru, and H. Ishiuchi, "An intelligent bipolar actuation method with high stiction immunity for RF MEMS capacitive switches and variable capacitors," *Sensors and Acuators A*, vol. 2007, pp. 233–236, 2007.

[20] D. Molinero and L. Castaner, "Comparison of airgap breakdown and substrate injection as mechanisms to induce charging in microelectromechanical switches," *Applied Physics Letters*, vol. 92, p. 43502, 2008.

[21] X. Yuan, S. Cherepko, J. Hwang, C. L. Goldsmith, C. Nordqusit, and C. Dyck, "Initial observation and analysis of dielectric-charging effects on RF MEMS capacitive switches," in *Digest of 2004 IEEE MTT-S International Microwave Symposium*, October 8 2004, pp. 1943 – 1946.

[22] X. Rottenberg, I. De Wolf, B. K. J. C. Nauwelaers, W. De Raedt, and H. A. C. Tilmans, "Analytical model of the DC actuation of electrostatic MEMS devices with distributed dielectric charging and nonplanar electrodes," *J. Microelectromech. Syst.*, vol. 16, pp. 1243–1253, 2007.

[23] W. M. Van Spengen, R. Puers, R. Mertens, and I. De Wolf, "A comprehensive model to predict the charging and reliability of capacitive RF MEMS switches," *Journal of Micromechanics and Microengineering*, vol. 14, pp. 514–521, 2004.

[24] R. W. Herfst, P. Steeneken, and J. Schmitz, "Time and voltage dependence of dielectric charging in RF MEMS capacitive switches," in *Proc. of IEEE 45th Annual International Reliability Physics Symposium, Phoenix, 2007*, 2007, pp. 417–421.

[25] M. Matmat, K. Koukos, F. Coccetti, T. Idda, A. Marty, C. Escriba, J.-Y. Fourniols, and D. Esteve, "Life expectancy and characterization of capacitive RF MEMS switches," *Microelectronics Reliability*, vol. 50, pp. 1692–1696, 2010.

[26] X.Yuan, J. C. M. Hwang, D. Forehand, and C. L. Goldsmith, "Modeling and characterization of dielectric-charging effects in RF MEMS capacitive switches," in *Digest of IEEE MTT-S 2005 Microwave Symposium Digest*, 2005, pp. 753–756.

[27] A. Grichener and G. Rebeiz, "Effects of dielectric charging on fundamental forces and reliability in capacitive microelectromechanical systems radio frequency switch contacts," *IEEE Trans. Microwave Theory Tech.*, vol. 58, pp. 2692–2701, 2010.

[28] S. Zafar, A. Callegari, E. Gusev, and M. V. Fischetti, "Charge trapping in high k gate dielectric stacks," in *Digest of International Electron Devices Meeting (IEDM 2002)*, December 8–11 2002, pp. 517–520.

[29] U. Zaghloul, G. Papaioannou, F. Coccetti, P. Pons, and R. Plana, "Dielectric charging in silicon nitride films for MEMS capacitive switches: Effect of film thickness and deposition conditions," *Microelectronics Reliability*, vol. 49, pp. 1309–1314, 2009.

[30] G. Papaioannou, M.-N. Exarchos, V. Theonas, G. Wang, and J. Papapolymerou, "Temperature study of the dielectric polarization effects of capacitive RF MEMS switches," *IEEE Trans. Microwave Theory Tech.*, vol. 53, pp. 3467–3473, 2005.

[31] G. J. Papaioannou, G. Wang, D. Bessas, and J. Papapolymerou, "Contactless dielectric charging mechanisms in RF-MEMS capacitive switches," in *Proc. of The First European Microwave Integrated Circuits Conference*, 2006, pp. 513–516.

[32] A. Koszewski, F. Souchon, C. Dieppedale, and T. Ouisse, "Modeling of dielectric charging in electrostatic MEMS switches," *Microelectronics Reliability*, vol. 50, p. 16091614, 2010.

[33] R. W. Herfst, H. G. A. Huizing, P. G. Steeneken, and J. Schmitz, "Characterization of dielectric charging in RF MEMS capacitive switches," in *Proc. of IEEE International Conference on Microelectronic Test Structures (ICMTS 2006)*, 2006, pp. 133–136.

[34] D. Molinero, "Study of dielectric charging effects on MEMS switches," Ph.D. dissertation, Technical University of Catalonia, Barcelona, 2009.

[35] H. Bruin and J. H. B. Deane, "Piecewise contractions are asymptotivally periodic," *Proceedings of the American Mathematical Society*, vol. 137, pp. 1389–1395, 2008.